Multiple-Scale Analysis of a Tunable Bi-Stable Piezoelectric Energy Harvester

Feng Qian
Department of Mechanical Engineering,
Virginia Tech,
Blacksburg, VA 24061
e-mail: fengqian@vt.edu

Nicole Abaid
Department of Mathematics,
Virginia Tech,
Blacksburg, VA 24061
e-mail: nabaid@vt.edu

Lei Zuo[1]
Department of Mechanical Engineering,
Virginia Tech,
Blacksburg, VA 24061
e-mail: leizuo@vt.edu

This paper presents the theoretical modeling and multiple-scale analysis of a novel piezoelectric energy harvester composed of a metal cantilever beam, piezoelectric films, and an axial preload spring at the moveable end. The harvester experiences mono- and bi-stable regimes as the stiffness of preload spring increases. The governing equations are derived with two high-order coupling terms induced by the axial motion. The literature shows that these high-order coupling terms lead to tedious calculations in the stability analysis of solutions. This work introduces an analytical strategy and the implementation of the multiple-scale method for the harvester in either the mono- or bi-stable status. Numerical simulations are performed to verify the analytical solutions. The influence of the electrical resistance, excitation level, and the spring pre-deformation on the voltage outputs and dynamics are investigated. The spring pre-deformation has a slight influence on the energy harvesting performance of the mono-stable system, but a large effect on that of the bi-stable system. [DOI: 10.1115/1.4046961]

Keywords: energy harvesting, nonlinear dynamics, mono-stable, bi-stable, method of multiple scales

1 Introduction

Considerable interest in vibration energy harvesting has emerged in the last decade with the rapid development of wireless sensors and low-power electrical devices [1–3]. Piezoelectric materials are extensively studied for mechanical-to-electrical energy conversion due to the high power densities and easy fabrication [4–6]. One critical issue of linear piezoelectric vibration energy harvesters (PEHs) is the limited frequency bandwidth [7,8]. A linear PEH needs to be deliberately designed to match its natural frequency with the excitation frequency to achieve resonance. A slight shift in the excitation frequency or any defects in the operation could lead to the frequency mismatch and thus a significant power reduction [9].

Nonlinearities are exploited to improve the operation frequency bandwidth, because nonlinear PEHs are insensitive to the change in excitation frequency due to the tilted frequency curves [10]. Nonlinear PEHs include mono-stable [1,4,9,11,12], bi-stable [13,14], and tri-stable harvesters [15,16]. Among them, bi-stable harvesters are preferable for their large power output during the larger-amplitude snap-through vibrations. Bi-stable PEHs have been shown to achieve a 300% improvement in the open-circuit root-mean-square voltage [17] and 13.1 times more power output [18]. Bi-stability can be realized by various mechanisms, such as repulsive magnets [19] and composite structures [20]. The nonlinearities usually make the analytical analysis become a daunting task, especially for systems with high-order coupling terms [21–23]. The harmonic balance method [11,12] has shown good accuracy for bi-stable systems. However, research shows the stability analysis of the harmonic balance solutions can be very complicated, even analytically impossible for systems with higher-order coupling terms [24]. On the other hand, the stability of multiple-scale solutions can be easily determined from the Jacobian matrix. Although the method of multiple scales [4,25,26] has been widely used for nonlinear systems, very few articles systematically apply this technique to systems with tunable potential wells and higher-order coupling terms. In particular, specific strategies are needed to handle the negative stiffness of bi-stable systems.

This letter presents the multiple-scale solutions of a broadband PEH with a tunable potential function, which consists of a metal cantilever beam, piezoelectric films, and an axial preload spring. The spring plays the similar role of repulsive magnets in literature to achieve the buckling mechanism. Advantages of this strategy lie in avoiding the magnetic interference with wireless sensor nodes and reducing the total mass [27]. The main contributions of this work include the following: (1) systematically introducing the technical strategies of the method of multiple scales for mono- and bi-stable systems; (2) obtaining the analytical frequency responses, phase angle, and phase portraits of the mono-stable and bi-stable systems; and (3) investigating the effect of the external resistance, excitation level, and the spring pre-deformation on the voltage outputs and dynamics of the systems.

2 Theoretical Model

Figure 1(*a*) shows the proposed PEH, where one end of the harvester is clamped and the other end connected to the spring is moveable along the guide rails. When the spring is compressed, the beam is exposed to the axial spring force. When the spring has a small pre-deformation, not enough to buckle the beam, the PEH is mono-stable; otherwise, the PEH enters into the bi-stable regime with two stable equilibria and one unstable equilibrium, as shown in Fig. 1(*a*). The two piezoelectric films on the beam are connected in parallel and the generated electricity is delivered to a resistive load. The PEH can be deemed as a current source and a capacitor [28], resulting in the simplified electrical circuit in Fig. 1(*b*). Assume the PEH experiences a base excitation of $\ddot{a} = A\cos(\Omega t)$, where t is time, A and Ω are the excitation level and frequency.

Let b and L be the width and length, h_s and h_p the thicknesses, ρ_s and ρ_p the densities of the beam and the piezoelectric films. The equivalent mass of per unit length is $m = \rho_s b h_s + 2\rho_p b h_p$. The effect of the electrode layers on the stiffness and mass is ignored because they are very thin and light. Let $w(x, t)$, $u(x, t)$, and $q(t)$ be the transverse, axial displacements, and the generated charge over the surfaces of the electrode layers. For simplicity, the transient displacement is approximated by the first mode as $w(x, t) = \eta(t)\varphi(x)$, where $\eta(t)$ is the first modal coordinate in the time domain and $\varphi(x) = [1 - \cos(2\pi x/L)]/2$ is the first mode shape function [18].

[1]Corresponding author.

Manuscript received October 24, 2019; final manuscript received February 18, 2020; published online May 11, 2020. Assoc. Editor: G. M. Clayton.

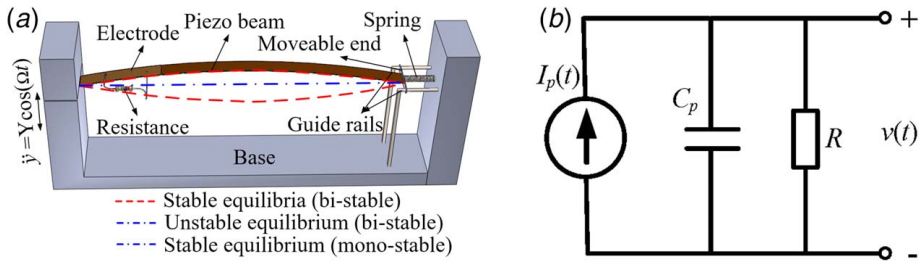

Fig. 1 (*a*) The nonlinear PEH and (*b*) equivalent electrical circuit

The inextensible assumption requires $(1+u')^2+w'^2=1$, and thus $u(x,t)=-1/2\int_0^x[w'(x,t)]^2dx$ [4,11,23], where the prime indicates the first derivative with respect to the coordinate x. The kinetic energy, potential energy, and work done by generalized forces are

$$T=\frac{m}{2}\int_0^L[\dot{\eta}^2\varphi^2(x)+2\dot{\eta}\dot{a}\varphi(x)+\dot{a}^2]dx+\frac{m}{2}(\eta\dot{\eta})^2\int_0^L\left(\int_0^x[\varphi'(x)]^2dx\right)^2dx \tag{1}$$

$$W=-c\eta\dot{\eta}\int_0^L\varphi^2(x)dx+q(t)v(t) \tag{2}$$

$$\begin{aligned}U=&\eta^2\left[\frac{EI}{2}\int_0^L[\varphi''(x)]^2dx-\frac{k_d\Delta}{2}\int_0^L[\varphi'(x)]^2dx\right]\\&+\eta^4\left[\frac{EA}{8}\int_0^L[\varphi'(x)]^4dx-\frac{k_d}{8}\left(\int_0^L[\varphi'(x)]^2dx\right)^2\right]\\&-\eta be_{31}v(t)(h_s+h_p)\int_0^{L_e}\varphi''(x)dx-\frac{1}{2}C_pv^2(t)\end{aligned} \tag{3}$$

where $E_3=-v(t)/h_p$ has been used and c denotes the damping coefficient. E_s and E_p are Young's modulus of the beam and the piezoelectric films, respectively. k_d and Δ are the stiffness and the pre-deformation of the spring. $EA=E_sbh_s+2E_pbh_p$ and $EI=E_sbh_s^3/12+E_pbh_p(4h_p^2+6h_ph_s+3h_s^2)/6$ are the equivalent axial and bending stiffness. $C_p=2\epsilon_{33}^sbL/h_p$ is the capacitance of the piezoelectric films. e_{31} and ϵ_{33}^s are the piezoelectric constant and relative permittivity measured at a constant strain. The governing equations are then extracted from the Lagrangian method as follows:

$$\ddot{\eta}+2\xi\omega_n\dot{\eta}+\beta(\eta\dot{\eta}^2+\eta^2\ddot{\eta})+(k_1-k_s)\eta+(k_2-k_3)\eta^3-\theta v=-\mu\ddot{a} \tag{4a}$$

$$\dot{v}+\lambda v+\bar{\theta}\dot{\eta}=0 \tag{4b}$$

where $\omega_n=\sqrt{k_1}$, and ξ is the mechanical damping ratio. The Gauss current law $\dot{q}(t)=I(t)=-v(t)/R$ has been used in the derivation of the electrical equation (4*b*). All the parameters in the governing equations are evaluated by

$$\xi=\frac{c}{2m\omega_n},\quad \beta=\frac{2\int_0^L\left(\int_0^x[\varphi'(x)]^2dx\right)^2dx}{m\int_0^L\varphi^2(x)dx},\quad k_1=\frac{EI\int_0^L[\varphi''(x)]^2dx}{m\int_0^L\varphi^2(x)dx},\quad k_s=\frac{k_d\Delta\int_0^L[\varphi'(x)]^2dx}{m\int_0^L\varphi^2(x)dx},$$

$$k_2=\frac{3EA\left(\int_0^L[\varphi'(x)]^2dx\right)^2}{8Lm\int_0^L\varphi^2(x)dx},\quad k_3=\frac{k_d\left(\int_0^L[\varphi'(x)]^2dx\right)^2}{8m\int_0^L\varphi^2(x)dx},\quad \theta=\frac{e_{31}b(h_s+h_p)\int_0^{l_e}\varphi''(x)dx}{4m\int_0^L\varphi^2(x)dx},$$

$$\mu=\frac{\int_0^L\varphi(x)dx}{\int_0^L\varphi^2(x)dx},\quad \lambda=\frac{1}{C_pR},\quad \bar{\theta}=\frac{e_{31}bh_p(h_s+h_p)}{4C_p}\int_0^{l_e}\varphi''(x)dx$$

Defining the dimensionless frequency and time $\omega=\Omega/\omega_n$ and $\tau=\omega_nt$, Eqs. (4*a*) and (4*b*) can be rearranged as

$$\eta''+2\xi\eta'+\beta[\eta(\eta')^2+\eta^2\eta'']+\chi\eta+\vartheta\eta^3-\alpha v=-\Lambda\cos(\omega\tau) \tag{5a}$$

$$v'+\bar{\lambda}v+\bar{\theta}\eta'=0 \tag{5b}$$

where the prime denotes the derivative with respect to τ, $\chi=(1-k_s/\omega_n^2)$, $\vartheta=(k_2-k_3)/\omega_n^2$, $\alpha=\theta/\omega_n^2$, $\bar{\lambda}=\lambda/\omega_n$, and $\Lambda=\mu A/\omega_n^2$. The governing equations have two higher-order coupling terms, the product of the displacement and squared velocity, and the product of the squared displacement and acceleration. Those terms significantly complicate the derivation of analytical solutions. Setting $\eta''=\eta'=0$ and ignoring the effect of electrical term, the equilibria can be obtained as

$$\eta_1^*=0,\quad \eta_{2,3}^*=\pm\sqrt{-\chi/\vartheta}=\pm\sqrt{-(k_1-k_s)/(k_2-k_3)} \tag{6}$$

The parameter ϑ is always positive because the scaled axial stiffness k_2 is much larger than the equivalent spring stiffness k_3. Thus, the existence of the equilibria $\eta_{2,3}^*$ depends on the effective spring stiffness k_s. The system has one equilibrium $\eta_1=0$ when Δ is small ($k_s<k_1$), and the PEH is mono-stable. As Δ increases to a certain level ($k_s=k_1$), the axial compressive force equals the critical buckling load of the beam. Then, the PEH begins to enter into the buckling regime.

The potential function is $\bar{V}(\eta)=\chi\eta^2/2+\vartheta\eta^4/4$, implying the parameter χ determines if the PEH is unbuckled or buckled. When $\chi>0$ ($k_s/k_1<1$), the harvester is unbuckled, otherwise, it is buckled bi-stable. Figure 2 plots the potential for the varying Δ with a constant spring stiffness of $k_d=1000$ N/m. The geometric and material properties of the PEH are listed in Table 1. The potential function has a flattened parabolic shape initially and turns to a double-well shape as Δ increases. This indicates the PEH turns from the mono-stable to the bi-stable state.

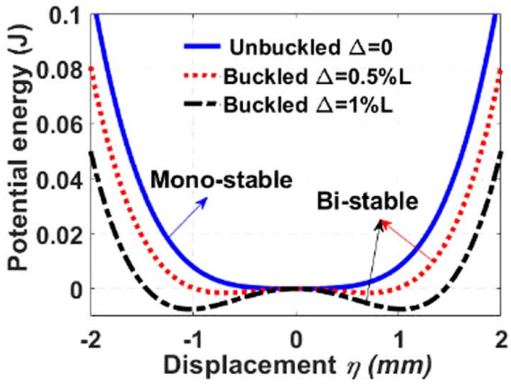

Fig. 2 Potential of the system with different spring pre-deformations

Table 1 The geometric and material properties of the PEH

Beam (steel) and spring		Piezoelectric layer	
Parameters	Value	Parameters	Value
Length, L	300 mm	Length, L_p	300 mm
Width, b	10 mm	Width, b	10 mm
Thickness, h_s	0.1 mm	Thickness, h_p	0.08 mm
Density, ρ_s	7850 kg m^{-3}	Density, ρ_p	4000 kg m^{-3}
Modulus, E_s	203 GPa	Modulus, E_p	40 GPa
Damping, ξ	0.042	d_{31}	-10 pC N^{-1}
Stiffness, k_d	2500 N m^{-1}	ε_{33}	8.854×10^{-10} F m^{-1}

3 Mono-Stable Piezoelectric Energy Harvester

To approximate the analytical solutions using the method of multiple scales, the damping term, nonlinear higher-order terms, cubic term, and the excitation are assumed to be small. Therefore, the mechanical equation (5*a*) can be written as

$$\eta'' + 2\varepsilon\xi\eta' + \varepsilon\beta[\eta(\eta')^2 + \eta^2\eta''] + \chi\eta + \varepsilon\vartheta\eta^3 - \varepsilon\alpha v = -\varepsilon\Lambda\cos(\omega\tau) \tag{7}$$

where ε is an small number. Introducing the fast and slow time variables $T_0 = \tau$ and $T_1 = \varepsilon\tau$, the solutions are expanded and retained to the first order of ε by the asymptotic series

$$\begin{cases} \eta(\tau) = \eta_0(T_0, T_1) + \varepsilon\eta_1(T_0, T_1) \\ v(\tau) = v_0(T_0, T_1) + \varepsilon v_1(T_0, T_1) \end{cases} \tag{8}$$

Substituting the multiple-scale solutions into Eqs. (7) and (5*b*), and equating the terms with the same order of ε yields

$$\begin{cases} \varepsilon^0{:}D_0^2\eta_0 + \chi\eta_0 = 0 \\ \varepsilon^1{:}D_0^2\eta_1 + \chi\eta_1 = -\Lambda\cos(\omega t) - 2D_0D_1\eta_0 - 2\xi D_0\eta_0 - \\ \beta[\eta_0(D_0\eta_0)^2 + \eta_0^2D_0^2\eta_0] - \vartheta\eta_0^3 + \alpha v_0 \end{cases} \tag{9}$$

$$\begin{cases} \varepsilon^0{:}D_0v_0 + \bar{\lambda}v_0 = -\bar{\theta}D_0\eta_0 \\ \varepsilon^1{:}D_0v_1 + \bar{\lambda}v_1 + \bar{\theta}D_0\eta_1 = -D_1v_0 - \bar{\theta}D_1\eta_0 \end{cases} \tag{10}$$

The solutions to the zeroth-order equations are assumed to be

$$\begin{cases} \eta_0 = A(T_1)e^{i\hat{\omega}T_0} + \bar{A}(T_1)e^{-i\hat{\omega}T_0} \\ v_0 = B(T_1)e^{i\hat{\omega}T_0} + \bar{B}(T_1)e^{-i\hat{\omega}T_0} \end{cases} \tag{11}$$

where $\hat{\omega} = \sqrt{\chi}$, $i = \sqrt{-1}$, A and B are the complex amplitudes and are functions of T_1. $\bar{A}$ and $\bar{B}$ are the complex conjugates of A and B. Substituting the solutions into the first equation in Eq. (10), the voltage amplitude can be expressed as

$$B = \bar{\theta}\hat{\omega}A/(-\hat{\omega} + i\bar{\lambda}) \text{ and } \bar{B} = -\bar{\theta}\hat{\omega}\bar{A}/(\hat{\omega} + i\bar{\lambda}) \tag{12}$$

Assume $\omega = \hat{\omega} + \varepsilon\sigma$, where σ is a detuning parameter. Substituting the resultant solutions into the second equation in Eq. (9) and setting the coefficients of the secular terms associated with $e^{i\hat{\omega}T_0}$ and $e^{-i\hat{\omega}T_0}$ to zeros, one has

$$\begin{cases} -\dfrac{\Lambda}{2}e^{i\sigma T_1} + 2i\hat{\omega}A' + 2\xi i\hat{\omega}A - (2\beta\hat{\omega}^2 - 3\vartheta)A^2\bar{A} - \alpha\dfrac{\bar{\theta}\hat{\omega}A}{-\hat{\omega} + i\bar{\lambda}} = 0 \\ -\dfrac{\Lambda}{2}e^{-i\sigma T_1} + 2i\hat{\omega}\bar{A}' + 2\xi i\hat{\omega}\bar{A} + (2\beta\hat{\omega}^2 - 3\vartheta)A\bar{A}^2 - \alpha\dfrac{\bar{\theta}\hat{\omega}\bar{A}}{\hat{\omega} + i\bar{\lambda}} = 0 \end{cases} \tag{13}$$

where $\cos[(\hat{\omega} + \varepsilon\sigma)\tau] = 1/2[e^{i(\hat{\omega}T_0 + \sigma T_1)} + e^{-i(\hat{\omega}T_0 + \sigma T_1)}]$ has been used. The prime denotes the derivative with respect to T_1.

Solving any of the two equations in Eq. (13) gives the solutions of the amplitude and phase angle. We assume the complex amplitudes have the following polar forms

$$A = \Gamma(T_1)/2e^{i\varphi(T_1)} \text{ and } \bar{A} = \Gamma(T_1)/2e^{-i\varphi(T_1)} \tag{14}$$

where Γ and φ are the amplitude and phase and are real functions of time T_1. Substituting Eq. (14) into the first equation in Eq. (13) and separating the real and imaginary parts yields

$$\begin{cases} \Gamma' = -\dfrac{\Lambda}{2\hat{\omega}}\sin(\sigma T_1 - \varphi) - \xi\Gamma - a_0\bar{\lambda}\Gamma \\ \Phi_0' = -\dfrac{\Lambda}{2\hat{\omega}\Gamma}\cos(\sigma T_1 - \varphi) + \sigma + a_1\Gamma^2 - a_0\hat{\omega} \end{cases} \tag{15}$$

where $\Phi_0 = \sigma T_1 - \varphi$, $a_0 = \alpha\bar{\theta}/[2(\hat{\omega}^2 + \bar{\lambda}^2)]$, $a_1 = (2\beta\hat{\omega}^2 - 3\vartheta)/(8\hat{\omega})$. By setting $\Gamma' = \Phi' = 0$, the frequency response function can be derived by

$$(\xi + a_0\bar{\lambda})^2 + (\sigma + a_1\Gamma^2 - a_0\hat{\omega})^2 = [\Lambda/(2\hat{\omega}\Gamma)]^2 \tag{16}$$

The corresponding phase angle is

$$\Phi_0 = \tan^{-1}[-(\xi + a_0\bar{\lambda})/(\sigma + a_1\Gamma^2 - a_0\hat{\omega})] \tag{17}$$

The amplitude Γ can be solved for different values of the detuning parameter σ from Eq. (16). The voltage amplitude can be attained from the second equation in Eq. (11), which is

$$V = \bar{\theta}\hat{\omega}\Gamma/\sqrt{\hat{\omega}^2 + \bar{\lambda}^2} \tag{18}$$

Multiple solutions of the amplitude Γ can be obtained from Eq. (16) for a given detuning parameter σ. These solutions include stable solutions in both high and low branches and unstable trivial solutions. The stability analysis of the solutions can be achieved by analyzing the real part of the eigenvalues of the Jacobian matrix. If the real parts of all the eigenvalues are negative, the solution is stable. Otherwise, it is unstable. The Jacobian matrix can be derived from Eq. (15) as

$$J = \begin{bmatrix} -(\xi + a_0\bar{\lambda}) & -\Gamma(\sigma + a_1\Gamma^2 - a_0\hat{\omega}) \\ \dfrac{1}{\Gamma}(\sigma + 3a_1\Gamma^2 - a_0\hat{\omega}) & -(\xi + a_0\bar{\lambda}) \end{bmatrix} \tag{19}$$

Eliminating the secular terms, the first-order solution can be obtained as

$$\eta_1 = (2\beta\hat{\omega}^2 - \vartheta)/(8\hat{\omega}^2)(A^3e^{3i\hat{\omega}T_0} + \bar{A}^3e^{-3i\hat{\omega}T_0}) \tag{20}$$

Plugging Eq. (14) into Eqs. (11) and (20), then substituting the results into Eq. (8), the approximate analytical solution of multiple

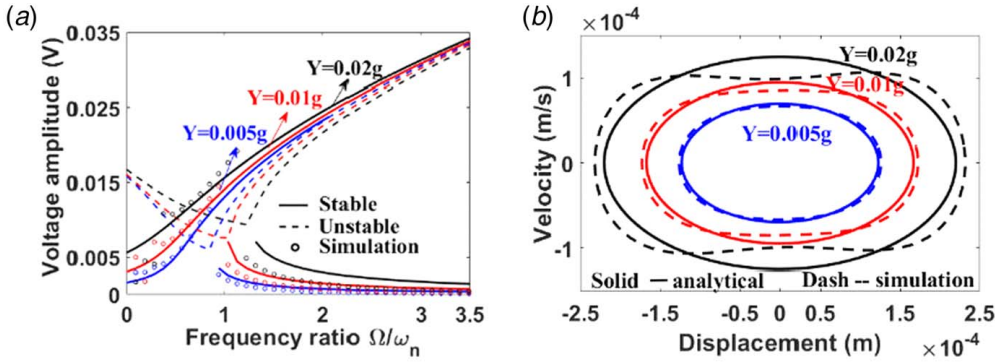

Fig. 3 (*a*) Voltage frequency responses of the mono-stable PEH and (*b*) phase portraits at $\omega = 0.57$

scales in the time domain can be written as

$$\eta(\tau) = \Gamma\cos(\omega\tau - \Phi) + \varepsilon\frac{(2\beta\hat{\omega}^2 - \vartheta)\Gamma^3}{32\hat{\omega}^2}\cos\,3(\omega\tau - \Phi) \tag{21}$$

where the relationship $\Phi = \sigma T_1 - \varphi$ has been used.

4 Case Study of the Mono-Stable Piezoelectric Energy Harvester

The voltage frequency responses are derived under three excitation levels of $Y = 0.005$ g, 0.01 g, and 0.02 g. To verify the analytical solutions, numerical simulations are conducted at discrete frequency points. The initial displacement, velocity, and voltage are assumed to be zeros. The preload spring is soft, limited to $k_s < k_1$ so that the PEH is mono-stable. Figure 3(*a*) presents the voltage frequency responses under the open-circuit condition, which has the typical characteristics of a mono-stable nonlinear system, consisting of high and low branches and tilting to the right hand. When the frequency is low ($\omega < 0.8$), the system has a single stable solution at the high branch, while two stable solutions concurrently appear at the low and high branches at the high frequency. The numerical simulations only get the low branch solutions in the frequency range of multiple stable solutions due to the zero initial conditions. The phase portraits at $\omega = 0.57$ are plotted in Fig. 3(*b*), which demonstrates the approximate solutions match well with the numerical simulations. Figure 4(*a*) shows the voltage frequency responses under different resistive loads at the excitation level of 0.005 g. Both the high and low branch VFRs decrease as the external resistance becomes smaller.

The effects of the excitation level and the spring pre-deformation on the voltage output are studied at two frequencies of $\omega = 0.4$ and 1.5. The spring pre-deformation is $\Delta = 0.05\%L$ for the case of varying excitation level. Figure 4(*b*) shows only the high branch oscillation happens at the small excitation frequency of $\omega = 0.4$ and the voltage increases along with the excitation level. Both the stable high and low branch solutions exist at lower excitation level ($Y = 0 \sim 0.3$ g) for $\omega = 1.5$. Figure 4(*c*) shows the voltage has a very slight increment as the spring pre-deformation increases for a fixed excitation level. This suggests that the spring pre-deformation has insignificant influence on the voltage output. This is because the linear and cubic stiffness of the mono-stable PEH is dominated by the bending and axial stiffness of the beam, when the spring pre-deformation is small.

5 Bi-Stable Piezoelectric Energy Harvester

As the effective spring stiffness k_s exceeds the scaled linear stiffness k_1, the overall linear stiffness χ becomes negative and the system enters into the bi-stable regime. The bi-stable PEH exhibits both small-amplitude intra-well oscillation and large-amplitude inter-well vibration. For the intra-well oscillation, a coordinate transform is performed to estimate the solutions around the local equilibria. For the inter-well oscillation, a strategy has to be taken to handle the negative stiffness. This section presents the strategies and solutions of the multiple scales for the approximate analytical analysis.

5.1 Intra-Well Oscillation. To analyze the intra-well dynamics, the original origin at the unstable equilibrium needs to be shifted to one of the stable equilibria $\eta^*_{2,3}$ [29]. Defining a new coordinate $y = \eta^*_{2,3} - \sqrt{-\chi/\vartheta}$ and substituting it into the governing Eq. (5*a*), one has

$$\begin{aligned} &y'' + 2\varepsilon^2\bar{\xi}y' - 2\bar{\chi}y + \varepsilon^2\bar{\beta}[(y+\kappa)(y')^2 + (y^2 + 2y\kappa)y''] \\ &\quad + 3\varepsilon\bar{\vartheta}\kappa y^2 + \varepsilon^2\bar{\vartheta}y^3 - \varepsilon^2\bar{\alpha}v = -\varepsilon^2\bar{\Lambda}\cos(\omega\tau) \end{aligned} \tag{22}$$

where $\bar{\xi} = \xi/[\varepsilon^2(1+\beta\kappa^2)]$; $\bar{\beta} = \beta/[\varepsilon^2(1+\beta\kappa^2)]$; $\bar{\chi} = \chi/(1+\beta\kappa^2)$; $\bar{\vartheta} = \vartheta/[\varepsilon^2(1+\beta\kappa^2)]$; $\bar{\alpha} = \alpha/[\varepsilon^2(1+\beta\kappa^2)]$; $\bar{\Lambda} = \Lambda/[\varepsilon^2(1+\beta\kappa^2)]$; $\kappa = \sqrt{-\chi/\vartheta}$. Introducing the multiple time variables $T_0 = \tau$, $T_1 = \varepsilon\tau$, and $T_2 = \varepsilon^2\tau$, the solutions can be approximated by the following asymptotic series:

$$\begin{cases} y(\tau) = y_0(T_0, T_1, T_2) + \varepsilon y_1(T_0, T_1, T_2) + \varepsilon^2 y_2(T_0, T_1, T_2) \\ v(\tau) = v_0(T_0, T_1, T_2) + \varepsilon v_1(T_0, T_1, T_2) + \varepsilon^2 v_2(T_0, T_1, T_2) \end{cases} \tag{23}$$

Plugging Eqs. (23) into (22), keeping the order to ε^2 and equating the like-order terms of ε, one has

$$\begin{cases} \varepsilon^0{:}D_0^2 y_0 - 2\bar{\chi}y_0 = 0 \\ \varepsilon^1{:}D_0^2 y_1 - 2\bar{\chi}y_1 = -2D_0D_1y_0 - 3\bar{\vartheta}\kappa y_0^2 \\ \varepsilon^2{:}2D_0D_1y_1 + 2D_0D_2y_0 + D_0^2y_2 + D_1^2y_0 - 2\bar{\chi}y_2 + \\ 2\bar{\xi}D_0y_0 + \bar{\beta}[y_0(D_0y_0)^2 + \kappa(D_0y_0)^2 + y_0^2D_0^2y_0 + \\ 2\kappa y_0D_0^2y_0] + \bar{\vartheta}y_0^3 + 6\bar{\vartheta}\kappa y_0y_1 - \bar{\alpha}v_0 = -\bar{\Lambda}\cos(\omega\tau) \end{cases} \tag{24}$$

Similarly, substituting the approximate solutions into Eq. (5*b*) and collecting the like-order terms of ε yield

$$\begin{cases} \varepsilon^0{:}D_0v_0 + \bar{\lambda}v_0 = -\bar{\theta}D_0y_0 \\ \varepsilon^1{:}D_0v_1 + \bar{\lambda}v_1 = -D_1v_0 - \bar{\theta}D_1y_0 - \bar{\theta}D_0y_1 \\ \varepsilon^2{:}D_0v_2 + \bar{\lambda}v_2 = -D_0y_2 - D_1y_1 - D_2y_0 - D_1v_1 - D_2v_0 \end{cases} \tag{25}$$

Assuming the solutions have the following forms:

$$\begin{cases} y_0(\tau) = A(T_1, T_2)e^{i\hat{\omega}T_0} + \bar{A}(T_1, T_2)e^{-i\hat{\omega}T_0} \\ v_0(\tau) = B(T_1, T_2)e^{i\hat{\omega}T_0} + \bar{B}(T_1, T_2)e^{-i\hat{\omega}T_0} \end{cases} \tag{26}$$

where $\hat{\omega} = \sqrt{-2\bar{\chi}}$; the complex amplitudes A and B, and their complex conjugates $\bar{A}$ and $\bar{B}$ depend on T_1 and T_2. Substituting

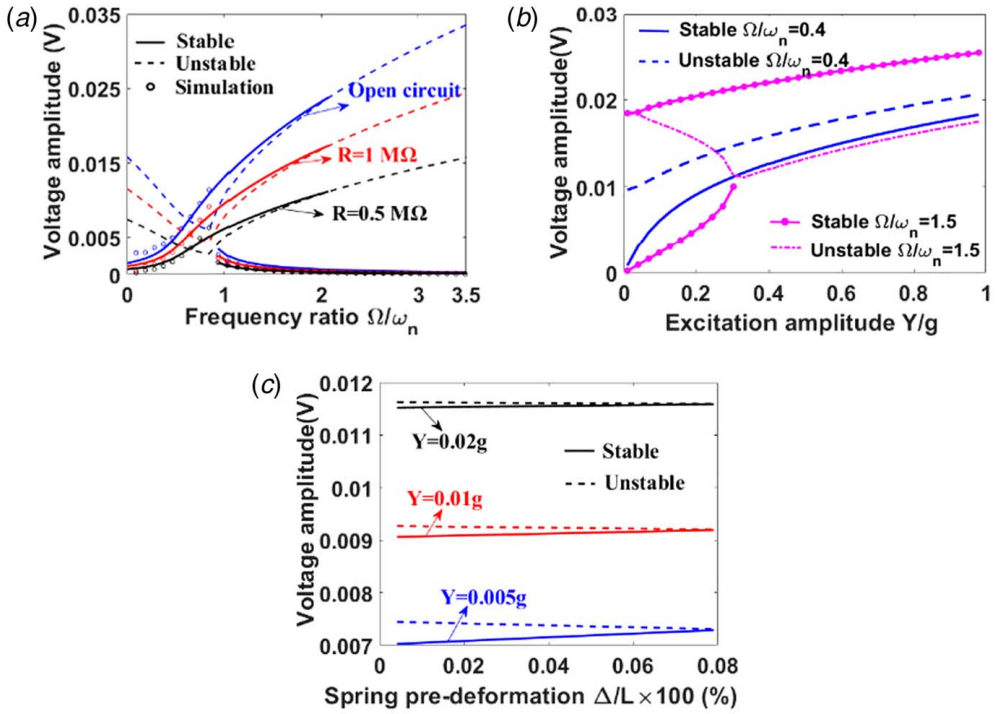

Fig. 4 Effects of (*a*) the electrical resistive load, (*b*) excitation level, and (c) spring pre-deformation on the voltage output

the solutions into the first-order equations, one has

$$D_0^2 y_1 - 2\bar{\chi} y_1 = 2i\hat{\omega}\left(-\frac{\partial A}{\partial T_1}e^{i\hat{\omega}T_0} + \frac{\partial \bar{A}}{\partial T_1}e^{-i\hat{\omega}T_0}\right) - 3\bar{\vartheta}\kappa(A^2 e^{i2\hat{\omega}T_0} + 2A\bar{A} + \bar{A}^2 e^{-i2\hat{\omega}T_0}) \tag{27}$$

Eliminating the secular terms yields $\partial A/\partial T_1 = \partial \bar{A}/\partial T_1 = 0$, implying A and $\bar{A}$ only depend on T_2, and solving Eq. (27) gives

$$y_1 = \frac{\bar{\vartheta}\kappa}{\hat{\omega}^2}(A^2 e^{i2\hat{\omega}T_0} + \bar{A}^2 e^{-i2\hat{\omega}T_0} - 6A\bar{A}) \tag{28}$$

Substituting the solutions into the second-order equation in Eq. (24), defining $\omega = \hat{\omega} + \varepsilon^2\sigma$, and setting the coefficients of the secular terms to zero, one has

$$\begin{cases} 2i\hat{\omega}A' + \left(2i\bar{\xi}\hat{\omega} - \dfrac{\bar{\alpha}\bar{\theta}\hat{\omega}}{-\hat{\omega} + i\bar{\lambda}}\right)A - \Psi\bar{A}A^2 + \dfrac{\bar{\Lambda}}{2}e^{i\sigma T_2} = 0 \\ 2i\hat{\omega}\bar{A}' + \left(2i\bar{\xi}\hat{\omega} - \dfrac{\bar{\alpha}\bar{\theta}\hat{\omega}}{\hat{\omega} + i\bar{\lambda}}\right)\bar{A} + \Psi A\bar{A}^2 - \dfrac{\bar{\Lambda}}{2}e^{-i\sigma T_2} = 0 \end{cases} \tag{29}$$

where $\Psi = \left(2\bar{\beta}\hat{\omega}^2 + 30\frac{(\bar{\vartheta}\kappa)^2}{\hat{\omega}^2} - 3\bar{\vartheta}\right)$. Both the above equations will give the same solution of A. Assuming $A = \Gamma(T_2)e^{i\varphi(T_2)}/2$ and $\bar{A} = \Gamma(T_2)e^{-i\varphi(T_2)}/2$, substituting into the first equation in Eq. (29), and setting the real and imaginary parts to zeros yield

$$\begin{cases} \Gamma' = -\bar{\xi}\Gamma - a_2\bar{\lambda}\Gamma - \bar{\Lambda}\sin\Phi_1/(2\hat{\omega}) \\ \Phi'_1 = \sigma - a_2\hat{\omega}^2 + a_3\Gamma^2 - \bar{\Lambda}\cos\Phi_1/(2\hat{\omega}\Gamma) \end{cases} \tag{30}$$

where $\Phi_1 = \sigma T_2 - \varphi$, $a_2 = \bar{\alpha}\bar{\theta}/[2(\hat{\omega}^2 + \bar{\lambda}^2)]$, and $a_3 = [2\bar{\beta}\hat{\omega}^2 + 30(\bar{\vartheta}\kappa)^2/\hat{\omega}^2 - 3\bar{\vartheta}]/(8\hat{\omega})$. Let $\Gamma' = \Phi'_1 = 0$, one can obtain the steady-state amplitude and phase angle as

$$[2\sigma - a_2\hat{\omega}^2 + 2a_3\Gamma^2]^2 + (2\bar{\xi} + a_2\bar{\lambda})^2 = \left(\frac{\bar{\Lambda}}{\hat{\omega}\Gamma}\right)^2 \tag{31}$$

$$\Phi_1 = \tan^{-1}[(-2\bar{\xi} - a_2\bar{\lambda})/2\sigma - a_2\hat{\omega}^2 + 2a_3\Gamma^2] \tag{32}$$

The voltage amplitude equation is the same as Eq. (18). The Jacobian matrix can be obtained from Eq. (30) as

$$J = \begin{bmatrix} -\bar{\xi} - a_2\bar{\lambda} & \Gamma(-\sigma + a_2\hat{\omega}^2 - a_3\Gamma^2) \\ (\sigma - a_2\hat{\omega}^2 + 3a_3\Gamma^2)/\Gamma & -\bar{\xi} - a_2\bar{\lambda} \end{bmatrix} \tag{33}$$

After eliminating the secular terms, one has

$$y_2 = \frac{-1}{(9\hat{\omega}^2 + 2\bar{\chi})}\left(2\bar{\beta}\hat{\omega}^2 - \bar{\vartheta} - \frac{6(\bar{\vartheta}\kappa)^2}{\hat{\omega}^2}\right)(A^3 e^{i3\hat{\omega}T_0} + \bar{A}^3 e^{-i3\hat{\omega}T_0}) - \frac{3\bar{\beta}\kappa\hat{\omega}^2}{2(2\hat{\omega}^2 + \bar{\chi})}(A^2 e^{i2\hat{\omega}T_0} + \bar{A}^2 e^{-i2\hat{\omega}T_0}) + \frac{2\bar{\beta}\kappa\hat{\omega}^2}{\bar{\chi}}A\bar{A} \tag{34}$$

Combing Eqs. (23), (26), (28), and (34), the approximate analytical solution can be obtained in the time domain as

$$y(\tau) = \Gamma\cos(\omega\tau - \Phi_1) + \varepsilon\frac{\bar{\vartheta}\kappa\Gamma^2}{2\hat{\omega}^2}[\cos 2(\omega\tau - \Phi_1) - 3] + \varepsilon^2\left[\frac{-\Gamma^3}{4(9\hat{\omega}^2 + 2\bar{\chi})}\left(2\bar{\beta}\hat{\omega}^2 - \bar{\vartheta} - \frac{6(\bar{\vartheta}\kappa)^2}{\hat{\omega}^2}\right)\cos 3(\omega\tau - \Phi_1) - \frac{3\bar{\beta}\kappa\hat{\omega}^2\Gamma^2}{4(2\hat{\omega}^2 + \bar{\chi})}\cos 2(\omega\tau - \Phi_1) + \frac{\bar{\beta}\kappa\hat{\omega}^2\Gamma^2}{2\bar{\chi}}\right] \tag{35}$$

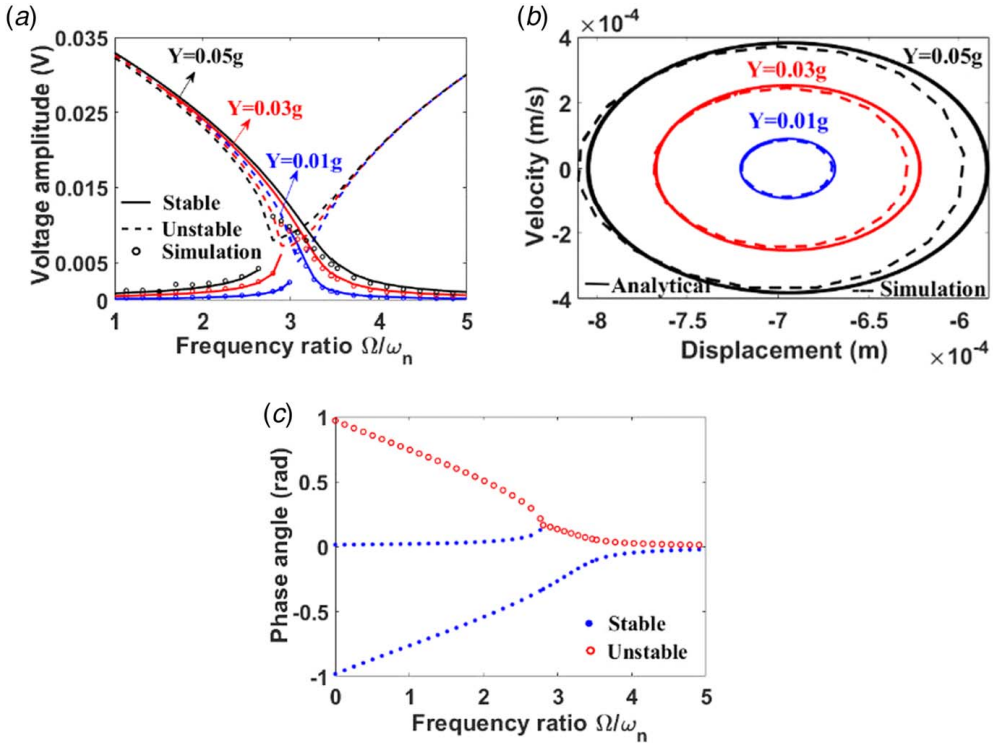

Fig. 5 Intra-well (*a*) voltage frequency responses, (*b*) phase portraits at $\omega = 3.46$, and (c) phase angle

5.2 Case Study of the Intra-Well Oscillation. The spring pre-deformation needs to satisfy $k_s > k_1$ to achieve the bi-stable configuration. Therefore, $\Delta = 0.5\%L$ is chosen in the following study unless otherwise stated. The analytical and numerical VFRs under the open-circuit condition are plotted in Fig. 5(*a*). The numerical results match with the analytical solutions. Different from that of the mono-stable PEH in Fig. 3(*a*), the intra-well VFRs of the bi-stable PEH bend to the left-hand side for the soft stiffness. The bi-stable PEH shows no advantage in voltage outputs compared with the mono-stable PEH at $Y = 0.01$ g.

The phase portraits at $\omega = 3.46$ and different excitation levels are presented in Fig. 5(*b*). The analytical solutions agree well with the numerical results. Figure 5(*b*) shows that the harvester is confined in one of the local potential wells. Figure 5(*c*) plots the phase angle along with the excitation frequency at $Y = 0.05$ g. The bifurcation can be observed from the phase angle as the excitation frequency varies.

The voltage frequency responses at different resistive loads are presented in Fig. 6(*a*) for $Y = 0.03$ g, which shows the resistive load has a significant influence on the voltage output. The voltage decreases as the resistive load dwindles. The voltage output is shown in Fig. 6(*b*) for varying excitation levels at $\omega = 2.9$ and 3.3. Unlike the case of the mono-stable PEH, only a single stable solution appears and augments as the excitation level becomes large at $\omega = 3.3$. For $\omega = 2.9$, the system has a single stable low branch solution under small excitation levels, but has two stable solutions of both high and low branches as the excitation level increases. There is only one stable high branch solution at high excitation levels.

The open-circuit voltage outputs at varying spring pre-deformations are plotted in Fig. 6(*c*) under the three excitation levels and $\sigma = 0$. The reason that the detuning parameter is set to zero is because the natural frequency of the system varies as the spring pre-deformation changes. Only one stable solution exists over the considered range of the spring pre-deformation. The voltage output decreases as the spring-deformation increases. We conclude that the spring-deformation has evident influence on the voltage output of the bi-stable PEH. This is attributed to the fact that the spring force has a remarkable contribution to the system stiffness.

5.3 Inter-Well Oscillation. Strategies are needed to handle the negative stiffness issue to apply the method of multiple scales. A fictitious positive stiffness term is introduced into Eq. (5*a*) to shift the linear negative stiffness to a positive one. By adding and subtracting the fictitious term $\hat{\omega}^2\eta$ to the left-hand side of Eq. (5*a*), one has

$$\eta'' + 2\varepsilon\xi\eta' + \hat{\omega}^2\eta + \varepsilon\beta[\eta(\eta')^2 + \eta^2\eta''] + \varepsilon[\bar{\chi}\eta + \vartheta\eta^3] - \varepsilon\alpha v = -\varepsilon\Lambda\cos(\omega\tau) \tag{36}$$

where $\hat{\omega} = \omega - \varepsilon\sigma$, and $\bar{\chi} = \chi - \hat{\omega}^2$. The damping, high-order terms, electrical coupling terms, excitation, and the stiffness terms $\bar{\chi}\eta + \vartheta\eta^3$ are assumed to be small. The solutions are assumed to be the same with those in Eq. (8). Substituting the solutions into Eqs. (36) and (5*b*), one has

$$\begin{cases} \varepsilon^0{:}D_0^2\eta_0 + \hat{\omega}^2\eta_0 = 0 \\ \varepsilon^1{:}D_0^2\eta_1 + \hat{\omega}^2\eta_1 = -\Lambda\cos(\omega\tau) - 2D_0D_1\eta_0 - 2\xi D_0\eta_0 \\ -\beta[\eta_0(D_0\eta_0)^2 + \eta_0^2D_0^2\eta_0] - \bar{\chi}\eta_0 - \vartheta\eta_0^3 + \alpha v_0 \end{cases} \tag{37}$$

$$\begin{cases} \varepsilon^0{:}D_0v_0 + \bar{\lambda}v_0 = -\bar{\theta}D_0\eta_0 \\ \varepsilon^1{:}D_0v_1 + \bar{\lambda}v_1 = -\bar{\theta}D_0\eta_1 - D_1\eta_0 - D_1v_0 \end{cases} \tag{38}$$

Substituting the zeroth-order solutions in Eq. (11) into the first equation in Eq. (38), one can find the relationship between the displacement and the voltage. Plugging the solutions into the second equation in Eq. (37), and setting the coefficients of the secular terms to zeros, and substituting the complex conjugate amplitudes

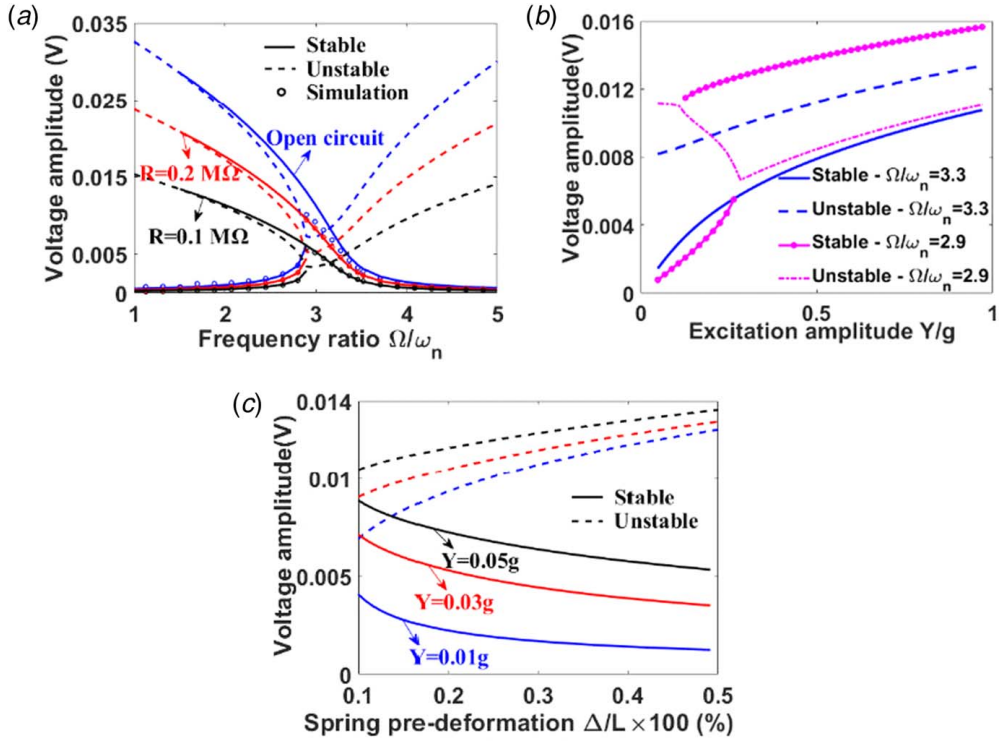

Fig. 6 Effect of the (*a*) electrical resistive load, (*b*) excitation level, and (*c*) spring pre-deformation on the voltage output

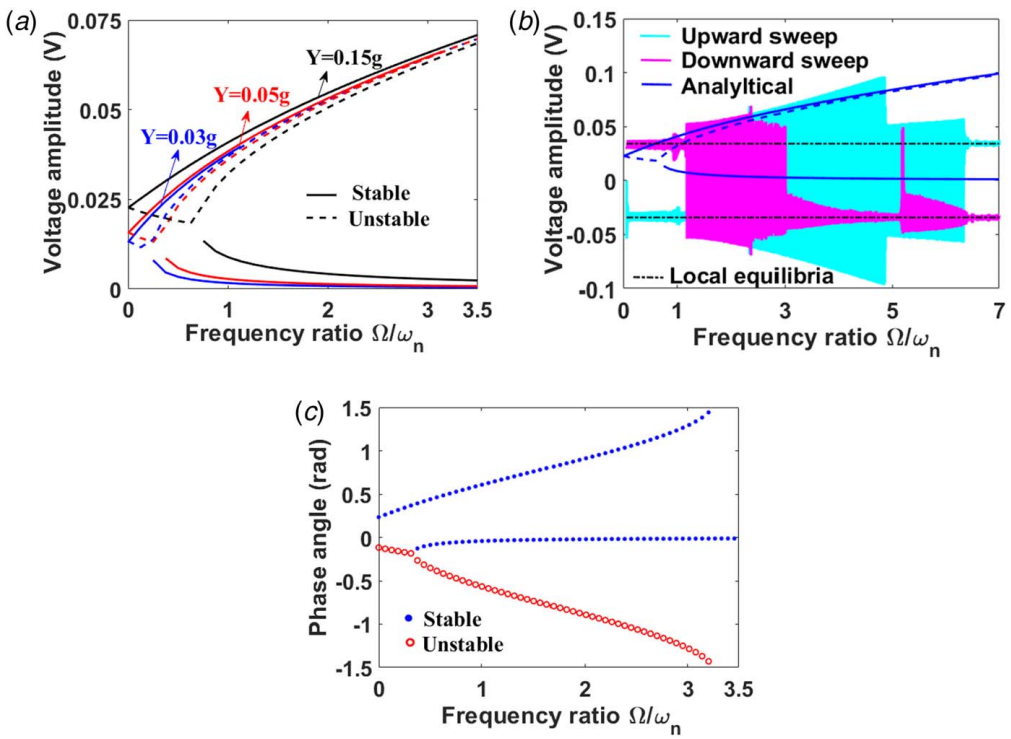

Fig. 7 Inter-well (*a*) voltage frequency responses, (*b*) numerical results and analytical solutions, and (*c*) phase angle

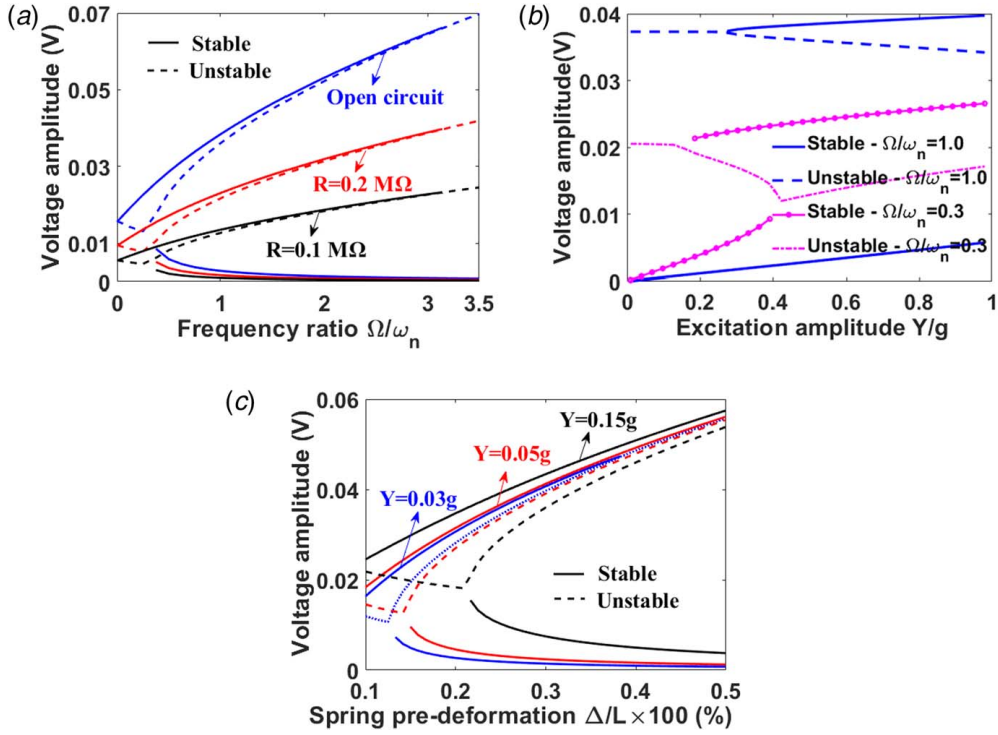

Fig. 8 Effect of the (*a*) external resistive load, (*b*) excitation level, and (*c*) spring pre-deformation on the voltage output

A and $\bar{A}$ into one of the resultant equation, one has

$$\begin{cases} \Gamma' = -\Lambda \sin \Phi_2/(2\hat{\omega}) - (\xi + a_0\bar{\lambda})\Gamma \\ \Phi'_0 = \sigma - \Lambda \cos \Phi_2/(2\hat{\omega}\Gamma) - [\bar{\chi}/(2\hat{\omega}) + a_0\hat{\omega}] + a_1\Gamma^2 \end{cases} \tag{39}$$

where Φ_0, a_0, and a_1 are defined in Sec. 3 and Γ is the real displacement amplitude. Let $\Gamma' = \Phi'_0 = 0$, one can obtain the steady-state amplitude and phase angle as

$$[2\hat{\omega} + \sigma - (\bar{\chi} + 2a_0\hat{\omega}^2) + 2a_1\hat{\omega}\Gamma^2]^2 + 4(\xi + a_0\bar{\lambda})^2\hat{\omega}^2 = [\bar{\Lambda}/(\hat{\omega}\Gamma)]^2 \tag{40}$$

$$\Phi_0 = \tan^{-1}\{-2(\xi + a_0\bar{\lambda})\hat{\omega}/[2\hat{\omega}\sigma - (\bar{\chi} + 2a_0\hat{\omega}^2) + 2a_1\hat{\omega}\Gamma^2]\} \tag{41}$$

The Jacobian matrix can be derived from Eq. (39) as follows:

$$J = \begin{bmatrix} -(\xi + a_0\bar{\lambda}) & -\Gamma\sigma + \Gamma(\bar{\chi}/2\hat{\omega} + a_0\hat{\omega}) - a_1\Gamma^3 \\ \dfrac{\sigma}{\Gamma} - \dfrac{1}{\Gamma}(\bar{\chi}/2\hat{\omega} + a_0\hat{\omega}) + 3a_1\Gamma & -(\xi + a_0\bar{\lambda}) \end{bmatrix} \tag{42}$$

The first-order solution η_1 is obtained after eliminating the secular terms. Together with the zeroth-order solution η_0, the analytical solution of the inter-well oscillation is

$$\eta = \Gamma\cos(\omega\tau - \Phi_0) - \varepsilon\frac{(2\beta\omega^2 - \vartheta)}{8\omega^2}\Gamma^3\cos 3(\omega\tau - \Phi_0) \tag{43}$$

5.4 Case Study of the Inter-Well Oscillation. The analytical voltage frequency responses at $Y = 0.03$ g, 0.05 g, and 0.15 g are presented in Fig. 7(*a*). The excitation levels are higher than those for the intra-well oscillations to activate the inter-well oscillation. Comparing the voltage frequency responses under $Y = 0.03$ g and 0.05 g in Fig. 7(*a*) with those in Fig. 5(*a*), it shows the inter-well oscillation outperforms the intra-well oscillation in voltage output. The numerical simulation results are not given in Fig. 7(*a*) as we did above because the inter-well oscillation cannot be always activated under the zero initial conditions.

To validate the analytical solution, upward and downward frequency sweeps are numerically performed to the governing equations within the frequency range of $\omega \in [0,7]$ and the excitation amplitdue of $Y = 0.15$ g. The numerical results are presented in Fig. 7(*b*) together with the analytical solutions. The amplitude of the numerical voltage response matches with the analytical solutions. Nevertheless, the analytical method overestimates the solutions at the higher frequency range. The numerical simulations are confined to the two local equilibria as the excitation frequency increases. The phase angle at the open circuit and $Y = 0.05$ g in Fig. 8(*b*) shows the bifurcation at $\omega = 0.32$.

The voltage frequency responses of the inter-well oscillation under $Y = 0.05$ g and different resistive loads are plotted in Fig. 8(*a*). Similarly, the voltage output becomes smaller as the external resistive load decreases. The voltage outputs over varying excitation levels are plotted in Fig. 8(*b*) for two frequencies of $\omega = 1.0$ and 0.3. The high voltage output from the large amplitude inter-well oscillation happens when the excitation level is greater than 0.27 g for $\omega = 1.0$. However, it is not available at the low excitation levels (0g $\sim$ 0.27 g) because of failing to activate the inter-well oscillation. For $\omega = 0.3$, the excitation amplitude has a similar influence on the voltage output with that of the intra-well oscillation. Figure 8(*c*) presents the voltage output over varying spring pre-deformations at the three excitation levels. The trend of the voltage outputs along with the varying spring pre-deformation is the same with these in Fig. 7(*a*). This is because the system stiffness is dominated by the effective spring stiffness k_s induced by the spring pre-deformation. The increase in the spring pre-deformation increases the linear stiffness.

6 Conclusion

A novel piezoelectric beam energy harvester with tunable potential function is developed and analytical modeled. An axial preload spring is connected to one moveable end of the beam to achieve the mono-stable or bi-stable systems. The method of multiple scales is systematically implemented to solve for the analytical frequency

responses and phase angles. To handle the negative stiffness, technical strategies are introduced to analyze the intra-well and inter-well dynamics. Numerical simulations are performed to confirm the analytical solutions. The effects of the electrical resistive load, excitation level, and spring pre-deformation on the dynamics and voltage output are studied. The voltage output of both the mono-stable and bi-stable systems increase along with the excitation level. The spring pre-deformation has slight influence on the energy harvesting performance of mono-stable system, but considerable effect on that of the bi-stable system.

Acknowledgment

This research was partially supported by National Science Foundation under Grants Nos. 1508862 and 1935951.

References

[1] Yang, Z., and Zu, J., 2016, "Toward Harvesting Vibration Energy From Multiple Directions by a Nonlinear Compressive-Mode Piezoelectric Transducer," IEEE/ASME Trans. Mechatron., **21**(3), pp. 1787–1791.
[2] Tang, L., and Wang, J., 2017, "Size Effect of Tip Mass on Performance of Cantilevered Piezoelectric Energy Harvester with a Dynamic Magnifier," Acta Mech., **228**(11), pp. 3997–4015.
[3] Qian, F., Zhou, W., Kaluvan, S., Zhang, H., and Zuo, L., 2018, "Theoretical Modeling and Experimental Validation of a Torsional Piezoelectric Vibration Energy Harvesting System," Smart. Mater. Struct., **27**(4), p. 045018.
[4] Abdelkefi, A., Nayfeh, A. H., and Hajj, M. R., 2012, "Global Nonlinear Distributed-Parameter Model of Parametrically Excited Piezoelectric Energy Harvesters," Nonlinear Dyn., **67**(2), pp. 1147–1160.
[5] Cao, Y., Huang, H., and He, W., 2019, "Energy Harvesting Characteristics of Preloaded Piezoelectric Beams," J. Phys. D: Appl. Phys., **53**(9), p. 095501.
[6] Xu, J., and Tang, J., 2015, "Multi-Directional Energy Harvesting by Piezoelectric Cantilever-Pendulum With Internal Resonance," Appl. Phys. Lett., **107**(21), p. 213902.
[7] Hu, H., Dai, L., Chen, H., Jiang, S., Wang, H., and Laude, V., 2017, "Two Methods to Broaden the Bandwidth of a Nonlinear Piezoelectric Bimorph Power Harvester," ASME J. Vib. Acoust., **139**(3), p. 031008.
[8] Pan, D., Ma, B., and Dai, F., 2017, "Experimental Investigation of Broadband Energy Harvesting of a Bi-Stable Composite Piezoelectric Plate," Smart. Mater. Struct., **26**(3), p. 035045.
[9] Abdelkefi, A., and Barsallo, N., 2016, "Nonlinear Analysis and Power Improvement of Broadband Low-Frequency Piezomagnetoelastic Energy Harvesters," Nonlinear Dyn., **83**(1–2), pp. 41–56.
[10] Daqaq, M. F., Masana, R., Erturk, A., and Quinn, D. D., 2014, "On the Role of Nonlinearities in Vibratory Energy Harvesting: A Critical Review and Discussion," ASME Appl. Mech. Rev., **66**(4), p. 040801.
[11] Fang, F., Xia, G., and Wang, J., 2018, "Nonlinear Dynamic Analysis of Cantilevered Piezoelectric Energy Harvesters Under Simultaneous Parametric and External Excitations," Acta Mech. Sin., **34**(3), pp. 561–577.
[12] Yang, Z., Zhu, Y., and Zu, J., 2015, "Theoretical and Experimental Investigation of A Nonlinear Compressive-Mode Energy Harvester With High Power Output Under Weak Excitations," Smart. Mater. Struct., **24**(2), p. 025028.
[13] Cao, J., Zhou, S., Inman, D. J., and Chen, Y., 2015, "Chaos in the Fractionally Damped Broadband Piezoelectric Energy Generator," Nonlinear Dyn., **80**(4), pp. 1705–1719.
[14] Zhou, S., Cao, J., Erturk, A., and Lin, J., 2013, "Enhanced Broadband Piezoelectric Energy Harvesting Using Rotatable Magnets," Appl. Phys. Lett., **102**(17), p. 173901.
[15] Haitao, L., Weiyang, Q., Chunbo, L., Wangzheng, D., and Zhiyong, Z., 2015, "Dynamics and Coherence Resonance of Tri-Stable Energy Harvesting System," Smart. Mater. Struct., **25**(1), p. 015001.
[16] Kim, P., Son, D., and Seok, J., 2016, "Triple-Well Potential With A Uniform Depth: Advantageous Aspects in Designing A Multi-Stable Energy Harvester," Appl. Phys. Lett., **108**(24), p. 243902.
[17] Xu, C., Liang, Z., Ren, B., Di, W., Luo, H., Wang, D., Wang, K., and Chen, Z., 2013, "Bi-stable Energy Harvesting Based on A Simply Supported Piezoelectric Buckled Beam," J. Appl. Phys., **114**(11), p. 114507.
[18] Cottone, F., Gammaiton, L., Vocca, H., Ferrari, M., and Ferrari, V., 2012, "Piezoelectric Buckled Beams for Random Vibration Energy Harvesting," Smart. Mater. Struct., **21**(3), p. 035021.
[19] Cottone, F., Vocca, H., and Gammaitoni, L., 2009, "Nonlinear Energy Harvesting," Phy. Rev. Lett., **102**(8), p. 080601.
[20] Li, H., and Qin, W., 2015, "Dynamics and Coherence Resonance of A Laminated Piezoelectric Beam For Energy Harvesting," Nonlinear Dyn., **81**(4), pp. 1751–1757.
[21] Tan, T., Yan, Z., Lei, H., and Sun, W., 2017, "Geometric Nonlinear Distributed Parameter Model for Cantilever-Beam Piezoelectric Energy Harvesters and Structural Dimension Analysis for Galloping Mode," J. Intell. Mater. Syst. Struct., **28**(20), pp. 3066–3078.
[22] Yan, Z., and Hajj, M. R., 2017, "Nonlinear Performances of an Autoparametric Vibration-Based Piezoelastic Energy Harvester," J. Intell. Mater. Syst. Struct., **28**(2), pp. 254–271.
[23] Firoozy, P., Khadem, S. E., and Pourkiaee, S. M., 2017, "Power Enhancement of Broadband Piezoelectric Energy Harvesting Using a Proof Mass and Nonlinearities in Curvature and Inertia," Int. J. Mech. Sci., **133**, pp. 227–239.
[24] Qian, F., Zhou, S., and Zuo, L., 2020, "Approximate Solutions and Their Stability of a Broadband Piezoelectric Energy Harvester With a Tunable Potential Function," Commun. Nonlinear Sci. Numer. Simul., **80**, p. 104984.
[25] Chen, L. Q., Jiang, W. A., Panyam, M., and Daqaq, M. F., 2016, "A Broadband Internally Resonant Vibratory Energy Harvester," ASME J. Vib. Acoust., **138**(6), p. 061007.
[26] Masana, R., and Daqaq, M. F., 2011, "Electromechanical Modeling and Nonlinear Analysis of Axially Loaded Energy Harvesters," ASME J. Vib. Acoust., **133**(1), p. 011007.
[27] Li, H. T., Qin, W. Y., Zu, J., and Yang, Z., 2018, "Modeling and Experimental Validation of A Buckled Compressive-Mode Piezoelectric Energy Harvester," Nonlinear Dyn., **92**(4), pp. 1–20.
[28] Yang, Z., Erturk, A., and Zu, J., 2017, "On the Efficiency of Piezoelectric Energy Harvesters," Extreme Mech. Lett., **15**, pp. 26–37.
[29] Harne, R. L., and Wang, K. W., 2017, *Harnessing Bistable Structural Dynamics: For Vibration Control, Energy Harvesting and Sensing*, John Wiley & Sons, Chichester, West Sussex, UK, pp. 58–62.